



Supplement of

Modeling dust mineralogical composition: sensitivity to soil mineralogy atlases and their expected climate impacts

María Gonçalves Ageitos et al.

Correspondence to: María Gonçalves Ageitos (maria.goncalves@upc.edu, maria.goncalves@bsc.es)

The copyright of individual parts of the supplement might differ from the article licence.

S1 Evaluation metrics and uncertainty estimates

The evaluation of the modeled dust surface concentration, dust deposition and mineral fractions against observations uses three different evaluation metrics: the normalized mean bias (nMB), eq. S1, the normalized root mean square error (nRMSE), eq. S2, and the Pearson's correlation (r), eq. S3, where M_i represents the modeled value at the observation location and time, O_i the corresponding observed value, N the number of observations considered, and \bar{M} and \bar{O} the mean values for the model and observations, respectively.

$$nMB = \frac{\sum_i M_i - O_i}{\sum_i O_i} \cdot 100 \quad (S1)$$

$$nRMSE = \frac{\sqrt{\frac{1}{N} \sum_i (M_i - O_i)^2}}{\bar{O}} \cdot 100 \quad (S2)$$

$$r = \frac{\sum_i (M_i - \bar{M}) \cdot (O_i - \bar{O})}{\sqrt{(\sum_i (M_i - \bar{M})^2 \cdot \sum_i (O_i - \bar{O})^2)}} \quad (S3)$$

- We use the three evaluation metrics described above with the aim of providing a quantitative assessment of our model skills when compared to observations. However, these statistical parameters are often derived from a limited set of observations, particularly when we address the evaluation of the mineral fractions. A key element of our work is the intercomparison of two model experiments that rely on different soil mineralogy maps, and the evaluation against mineralogy observations provides relevant information to assess the strengths and weaknesses of these datasets. Relying exclusively on the mean values of the nMB, nRMSE and r to compare the two model experiments could be misleading, specially for those cases with a low number of observations. Therefore, we incorporate to our assessment the information of the number of data points that are available to produce these metrics and their uncertainty ranges at a 95% confidence level, as described below. We assume that the performance of our two experiments is statistically distinct for an evaluation metric (nMB, nRMSE, or r) whenever its mean value for one of the experiments falls outside the uncertainty range estimated for the other.

- For the nMB we estimate the uncertainty range (nMB_{int}) using a two tailed Student t-test, as in eq. S4, with sd_{nMB} the standard deviation of the nMB and N the number of points considered. The degrees of freedom (df) to define the critical value (qt) are N-1, and the probability levels (p), 0.025 and 0.975.

$$nMB_{int} = qt(p, df) \cdot \frac{sd_{nMB}}{\sqrt{N}} \quad (S4)$$

- For the nMRSE, a chi-squared statistic is used, thus the uncertainty levels ($nRMSE_{int}$) can be calculated as in eq. S5, where qx is the critical value for N degrees of freedom (df) and the probability levels (p) of 0.025 and 0.975.

$$nRMSE_{int} = \sqrt{\frac{N}{qx(p, df)}} \quad (S5)$$

Finally, for the correlation, a Fisher transformation is applied to create a normal variable. The uncertainty range is assessed for the normally distributed values assuming a two-sided confidence of 95% (critical value of 1.96). Then the transformation is reversed for the calculated bounds to obtain the uncertainty range of r .

30 **S2 Processing the observational database of mineral fractions in dust samples**

The observations of mass mineral fractions compiled by Perlwitz et al. (2015) are used in this study for model evaluation purposes. To avoid using observations that might be contaminated with minerals of anthropogenic origin (i.e., from combustion or industrial activities) we apply a spatial filter to the dataset. The mask to remove the anthropogenic influence is derived from a multi-annual experiment conducted with the Community Atmosphere Model version 5 (Hamilton et al., 2019) at the global
35 scale, that represents the atmospheric iron cycle and considers dust, anthropogenic combustion and biomass burning iron sources. We define as prominently dusty those areas where the fractional contribution of dust to the total iron is of 75% or larger (see Figure S1). Observations that fall in regions with contributions of combustion sources larger than 25% to the total iron are removed from our comparison.

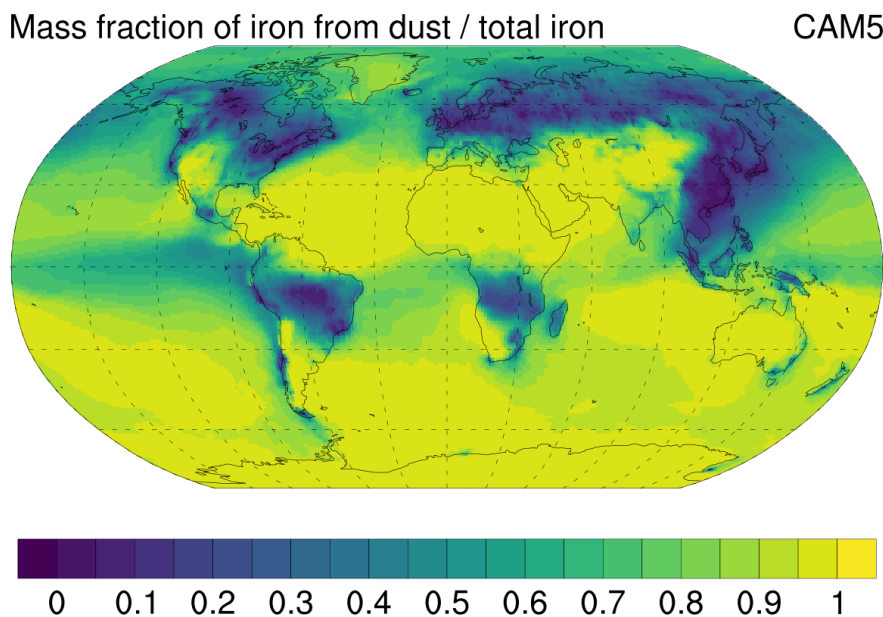


Figure S1. Mass fraction of iron from dust relative to total iron as simulated by the CAM5 model. The 0.75 threshold is used to filter the mineral fraction observations, values below 0.75 represent regions with a relevant contribution of anthropogenic sources to mineralogy, values above are assumed to happen in regions primarily influenced by dust

In addition, the observational database includes for each sample a number of minerals that are not explicitly represented in
40 MONARCH, but that are in some cases similar in structure and/or physico-chemical properties to those modeled, i.e. they are considered as equivalent and belonging to the same mineralogical family.

Therefore, a first step in the evaluation process is to create a correspondence between the observed and the modeled minerals and re-calculate the mean mass fraction and standard deviation for each of the samples reported. We select as modeled minerals those in C1999-SMA and J2014-SMA, and add an additional category of *Other* to include the remaining observed minerals
 45 that are not traced by the model. In the case of some clays (e.g. kaolinite and chlorite) that are reported together, the values are kept whenever those are modeled. For the iron oxides, we decide to keep the values of hematite when reported, independently. We further assume that iron oxides may include hematite, goethite, magnetite or others, and we will compare them with the iron oxides traced in our model. The minerals' correspondence is shown in table S1.

To estimate the mean mass fraction of the lumped minerals we sum up the mass fraction of the different individually
 50 reported minerals. To estimate the standard deviation of the re-calculated mean, we assume the mineral measurements to be non correlated, and therefore the new standard deviation for a mineral group (i) is calculated as the square root of the sum of variance of the n independently reported minerals (j), as in equation S6.

$$\sigma_i = \sqrt{\sum_{j=1}^n \sigma_j^2} \quad (S6)$$

Table S1. Association between reported minerals in observations and modeled MONARCH minerals for evaluation purposes.

Modeled mineral	C1999	J2014	Observed minerals
Illite	x	x	Illite, Fe-illite, Iron rich illite, Mica-illite
Smectite	x	x	Smectite, Montmorillonite
Kaolinite	x	x	Kaolinite
Chlorite	x	x	Chlorite, Clinochlore, Al-Chlorite
Vermiculite	x	x	Vermiculite
Illite-montmorillonite	x	x	Illite Smectite Mixed layers, Interstratified illite-smectite, Illite and mixed layer illite-smectite
Kaolinite-Chlorite	x	x	Kaolinite-Chlorite
Feldspars	x	x	Feldspars, Albite, Ca-Na-Feldspar, K-Feldspar, Microcline, Na-Feldspar, Orthoclase, Plagioclase, Other feldspar
Quartz	x	x	Quartz
Calcite	x	x	Calcite, Dolomite, Carbonates, Calcite and dolomite, Mg calcite
Hematite	x	x	Hematite
Goethite	x	x	Goethite
Iron oxides	x	x	Iron oxides, Hematite, Goethite, Fe-Ti oxides, Magnetite
Mica	x	x	Mica, Muscovite
Gypsum	x	x	Gypsum

S3 Refractive indexes for dust and mineral components

- 55 The SSA in the visible band shown in Section 6 of the main article is diagnosed using an average of the refractive indices depicted in Fig. S2 and Table S2. Values for dust are taken from Sinyuk et al. (2003), while the mineral components are inferred from the reported values in Di Biagio et al. (2017, 2019) and the specific mineral refractive indexes in Scanza et al. (2015), as explained in the main text.

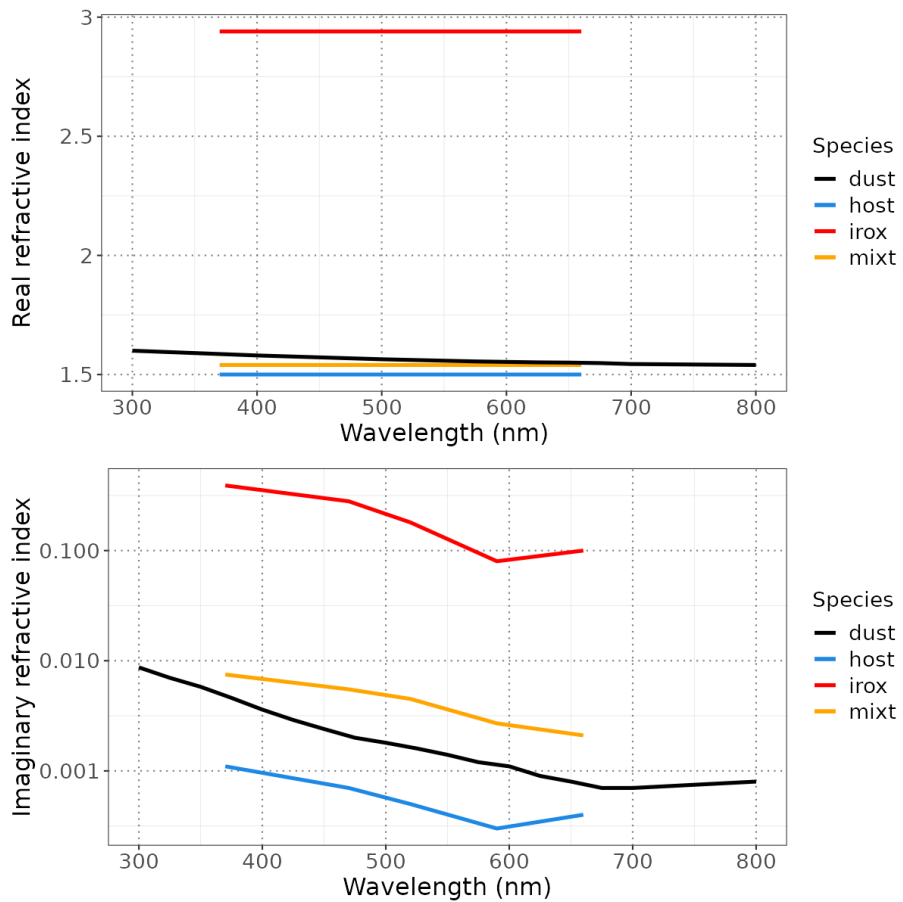


Figure S2. Real and imaginary part of the refractive index used in this work for compositionally homogeneous dust, externally mixed iron oxides, host minerals and mixtures of iron oxides and host minerals (see main text for details).

Table S2. Real (rri) and imaginary (iri) part of the refractive indices for dust and the different mineral components used in this study for visible wavelengths (wv)

Dust			Mineral components						
			Host		Mixtures		Iron oxides		
wv (nm)	rri	iri	wv (nm)	rri	iri	rri	iri	rri	iri
300	1.600	0.0087							
325	1.595	0.0070							
350	1.590	0.0058							
375	1.585	0.0046	370	1.50	0.0011	1.54	0.0075	2.94	0.39
400	1.580	0.0036							
475	1.576	0.0029							
450	1.572	0.0024							
475	1.568	0.0020	470	1.50	0.0007	1.54	0.0055	2.94	0.28
500	1.564	0.0018							
525	1.561	0.0016	520	1.50	0.0005	1.54	0.0045	2.94	0.18
550	1.558	0.0014							
575	1.555	0.0012							
600	1.553	0.0011	590	1.50	0.0003	1.54	0.0027	2.94	0.08
625	1.551	0.0009							
650	1.550	0.0008	660	1.50	0.0004	1.54	0.0021	2.94	0.10
675	1.548	0.0007							
700	1.544	0.0007							
800	1.540	0.0008							

The real part of the refractive index for the mineral components is taken as an average of those inferred from Di Biagio et al. (2017, 2019) for the purpose of the calculations in this study, therefore a common value is reported for all wavelengths in this table.

S4 Results of the bulk dust evaluation

- 60 Table S3 presents the evaluation statistics for the comparison of the modeled dust surface concentration against RSMAS and AMMA climatologies, and dust deposition fluxes against observations for present climate compiled in Albani et al. (2014).

Table S3. Number of stations (n), normalized mean bias (nMB, %), normalized root mean square error (nRMSE, %), and correlation (r) from the comparison of modeled annual mean dust surface concentration against RSMAS and AMMA observations, and modeled annual mean dust deposition against observations in Albani et al. (2014). To match the observed size range estimates of modeled values below 10 μm in diameter are used. Numbers in parenthesis represent the ranges of the statistical scores with a 95% confidence level (see section 1 in this document for details). Regions are identified in Figure 2 of the main article.

Region	Dust surface concentration					Dust deposition flux				
	n	nMB (%)	nRMSE (%)	r	n	nMB (%)	nRMSE (%)	r		
NAmer	1	-32.7	32.7		7	-85.9 (-98.4,-73.3)	118.9 (78.6,241.9)		0.60 (-0.28,0.93)	
CAmer	2	28.5	43.5		3	-22.5	50.4		0.97	
SAmer					1	-93.8	93.8			
Europe	2	-95.2	119.0		14	-51.3 (-55.5,47.1)	105.5 (77.2,166.3)		0.46(-0.09,0.80)	
NAfri	4	17.3	54.7	0.92	23	-50.1 (-52.7,47.5)	127.6 (99.1,178.9)		0.66(0.34,0.84)	
SAfri										
WAsMe	5	-60.8	86.1	-0.66						
		-77.8 (-114.6,-40.9)	159.6 (99.6,391.4)	-0.40 (-0.95,0.74)						
EAsia	2	-43.2	43.3		14	-48.3 (-59.6,-37.0)	171.9 (125.8,271.0)		1.00 (0.99,1.00)	
AusOc	3	-77.8	115.8	0.96	9	-97.5 (-113.6,-81.5)	199.4 (137.1,364.0)		0.88 (0.53,0.98)	
SPac	3	-70.4	73.0	0.95	2	-90.9	92.5			
NPac	4	-3.4	18.8	0.95	13	-84.2 (-90.1,-78.3)	141.5 (102.6,227.9)		0.60 (0.08,0.87)	
SOce	2	-98.4	113.0		15	-30.8 (-37.2,-24.3)	108.4 (80.1,167.7)		0.96 (0.88,0.99)	
Global	23	11.7 (8.0, 15.4)	116.1 (90.2,162.8)	0.95 (0.88, 0.98)	110	-57.3 (-57.7,-56.9)	210.7 (186.2,242.8)	0.80 (0.72, 0.86)		

For regions with 4 or less points the scores are to be interpreted as qualitative and not statistically significant according to our analyses.

S5 Annual mean budgets for minerals at emission, atmospheric burden and deposition

Table S4 presents the annual average of the global emission, burden, dry, wet and total deposition per mineral as estimated in the C1999 and J2014 experiments presented in the main paper.

Table S4. Emission, atmospheric burden and deposition global budgets (Tg). Lifetime (days). Annual mean over 2006-2010. quar: quartz, calc: calcite, feld: feldspar, gypsum, illi: illite, kaol: kaolinite, smec: smectite, irox: iron oxides, chlo: chlorite, verm: vermiculite, mica: mica, hema: hematite, goet: goethite, phyl: phyllosilicates, and othr: other.

C1999		quar	calc	feld	gyps	illi	kaol	smec	chlo	verm	mica	hema	goet	phyl	irox	othr	dust
Emission		1359.6	181.8	451.9	47.2	617.6	428.9	339.5				56.0	1386.0	56.0		3458.6	
Burden		9.8	1.3	3.3	0.4	5.8	4.3	3.1				0.5	13.2	0.5		28.5	
Dry deposition		820.1	109.1	273.3	27.1	342.4	229.2	188.7				31.4	760.4	31.4		2021.3	
Wet deposition		511.2	68.5	169.5	18.9	255.7	186.4	140.1				23.2	582.2	23.2		1373.6	
Total deposition		1331.3	177.6	442.9	46.0	598.1	415.6	328.8				54.6	1342.5	54.6		3394.8	
Lifetime		2.7	2.7	2.8	3.0	3.5	3.7	3.5				3.2	3.6	3.2		3.1	

J2014		quar	calc	feld	gyps	illi	kaol	smec	chlo	verm	mica	hema	goet	phyl	irox	othr	dust
Emission		1097.0	289.8	373.0	3.9	463.1	430.5	338.0	179.9	43.2	173.3	19.1	47.9	1628.1	67.0		3458.8
Burden		7.8	2.3	2.7	0.0	4.4	4.1	3.2	1.5	0.4	1.2	0.2	0.4	14.8	0.6		28.3
Dry deposition		659.6	170.1	228.1	2.1	251.2	237.4	185.8	105.0	23.9	107.2	10.8	27.1	910.5	38.0		2008.4
Wet deposition		414.8	112.7	137.6	1.7	196.8	179.5	141.8	70.8	17.9	62.9	7.7	19.4	669.7	27.1		1363.7
Total deposition		1074.4	282.8	365.7	3.7	448.0	416.9	327.6	175.8	41.9	170.1	18.5	46.6	1580.2	65.1		3372.1
Lifetime		2.7	3.0	2.7	2.6	3.6	3.6	3.6	3.0	3.7	2.6	3.6	3.2	3.4	3.4		3.1

J2014NN		quar	calc	feld	gyps	illi	kaol	smec	chlo	verm	mica	hema	goet	phyl	irox	othr	dust
Emission		971.5	256.2	334.5	3.0	424.0	405.2	304.3	162.1	41.5	154.4	18.4	43.8	1491.6	62.2	339.7	3458.8
Burden		7.0	2.1	2.5	0.0	4.0	3.9	2.9	1.3	0.4	1.1	0.2	0.4	13.7	0.6	2.6	28.3
Dry deposition		584.5	151.0	204.5	1.6	230.6	224.3	168.1	94.6	23.1	95.8	10.5	24.8	836.4	35.3	195.1	2008.5
Wet deposition		366.9	99.0	123.4	1.3	179.6	168.2	126.9	63.7	17.2	55.8	7.4	17.8	611.4	25.1	136.4	1363.5
Total deposition		951.4	250.0	328.0	2.9	410.2	392.5	295.0	158.3	40.2	151.5	17.8	42.6	1447.8	60.4	331.5	3372.0
Lifetime		2.7	3.0	2.7	2.6	3.6	3.6	3.6	3.1	3.7	2.6	3.6	3.3	3.4	3.4	3.1	

65 S6 Relative differences in surface concentration of phyllosilicates between C1999 and J2014

Figure S3 shows the comparison of phyllosilicate mass fractions between the experiments of C1999 and J2014, including mica as part of the illite-like minerals.

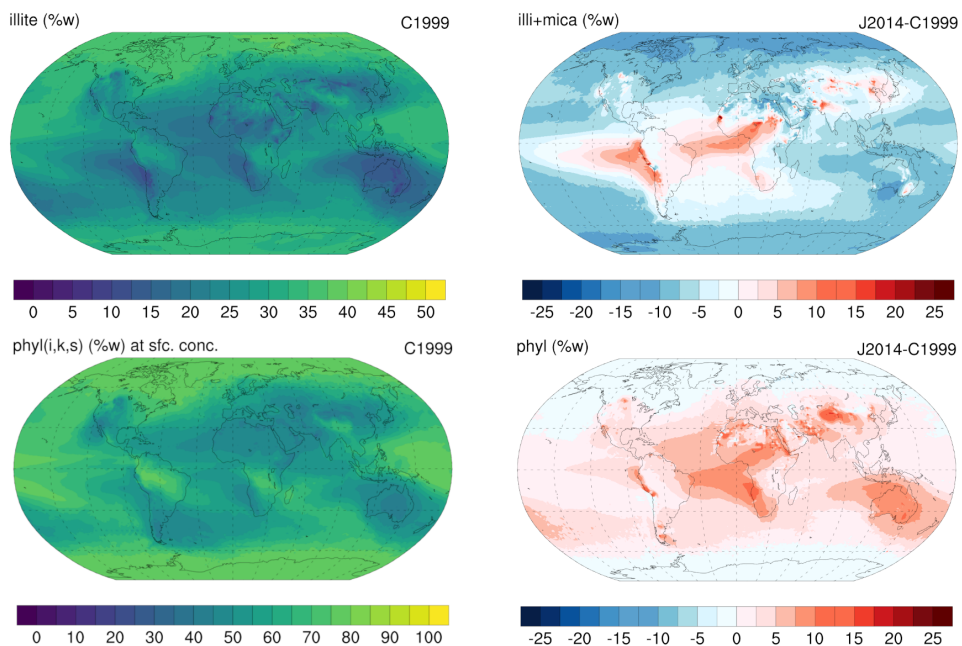


Figure S3. Mass fraction of illite and phyllosilicates:illite, kaolinite and smectite (%w) at the surface in C1999 (left) and differences (%w) bewteen J2014 illite and mica (up) and phyllosilicates: illite, kaolinite, chlorite, vermiculite and smectite (right).

S7 Diagnostics and evaluation of total iron for J2014NN

Figure S4 represents the total annual mean deposition estimated from the MONARCH J2014NN experiment and the differences with respect to the C1999 estimates. Figure S5 presents the evaluation of the predicted surface concentration of total iron from J2014NN against the observations compiled in Myriokefalitakis et al. (2018).

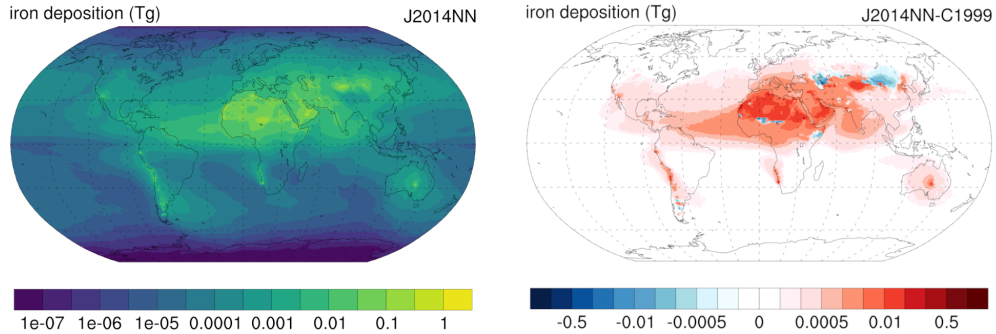


Figure S4. Total iron deposition (Tg yr^{-1}) as estimated from J2014NN mineralogy (left) and differences with respect to C1999 (right).

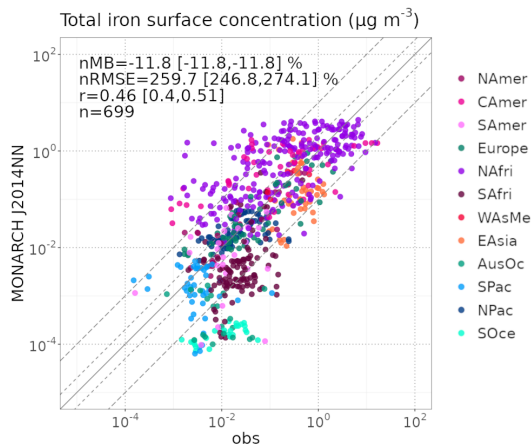


Figure S5. Diagnostic of the total iron surface concentration ($\mu\text{g m}^{-3}$) associated to the MONARCH modeled J2014NN dust mineralogy compared the observations compiled in Myriokefalitakis et al. (2018) identified as dust-dominated (see Fig. 1c and Section 4.4 in the main paper). Where n is the number of measurements, nRMSE, the normalized Mean Root Square Error, nMB, the normalized Mean Bias, and r, the correlation, over all points. The ranges for the nMB, nRMSE and r correspond to the 95% confidence level (see Section 1 of the Supplement for details). Regions are depicted in Figure 1c. Ashed lines represent differences of 2 times and one order of magnitude.

S8 C1999-SMA and J2014-SMA Soil Mineralogy Atlas

Figures S6 to S11 represent the global distribution of the mineral mass fractions in the clay and silt sizes of the soil as derived from C1999-SMA and J2014-SMA at $0.5 \times 0.5^\circ$ resolution. The description of these datasets can be found in the Appendix A of the main article.

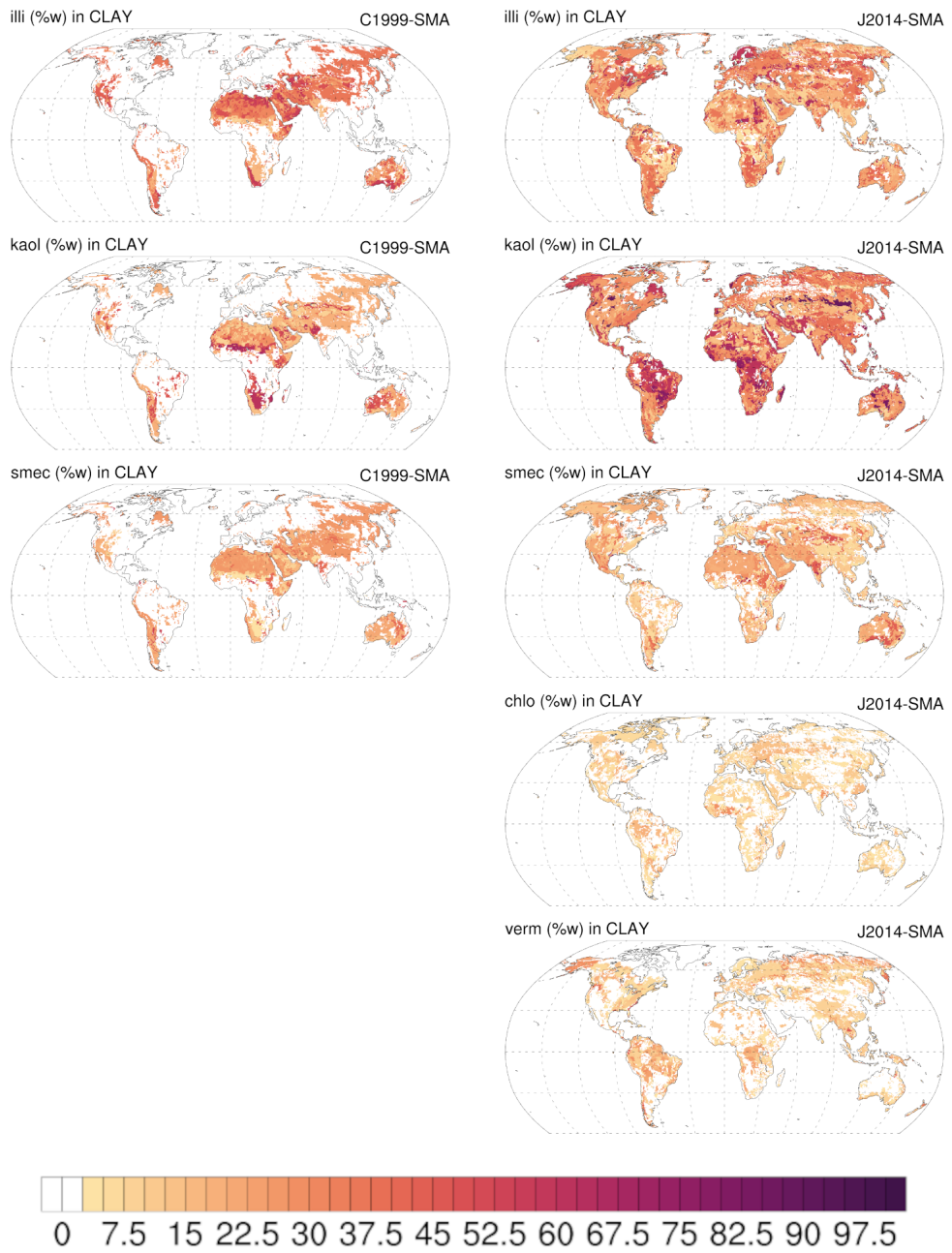


Figure S6. Mass fraction of phyllosilicates (%w) in the clay sizes of the soil according to C1999-SMA -left- and J2014-SMA -right-.

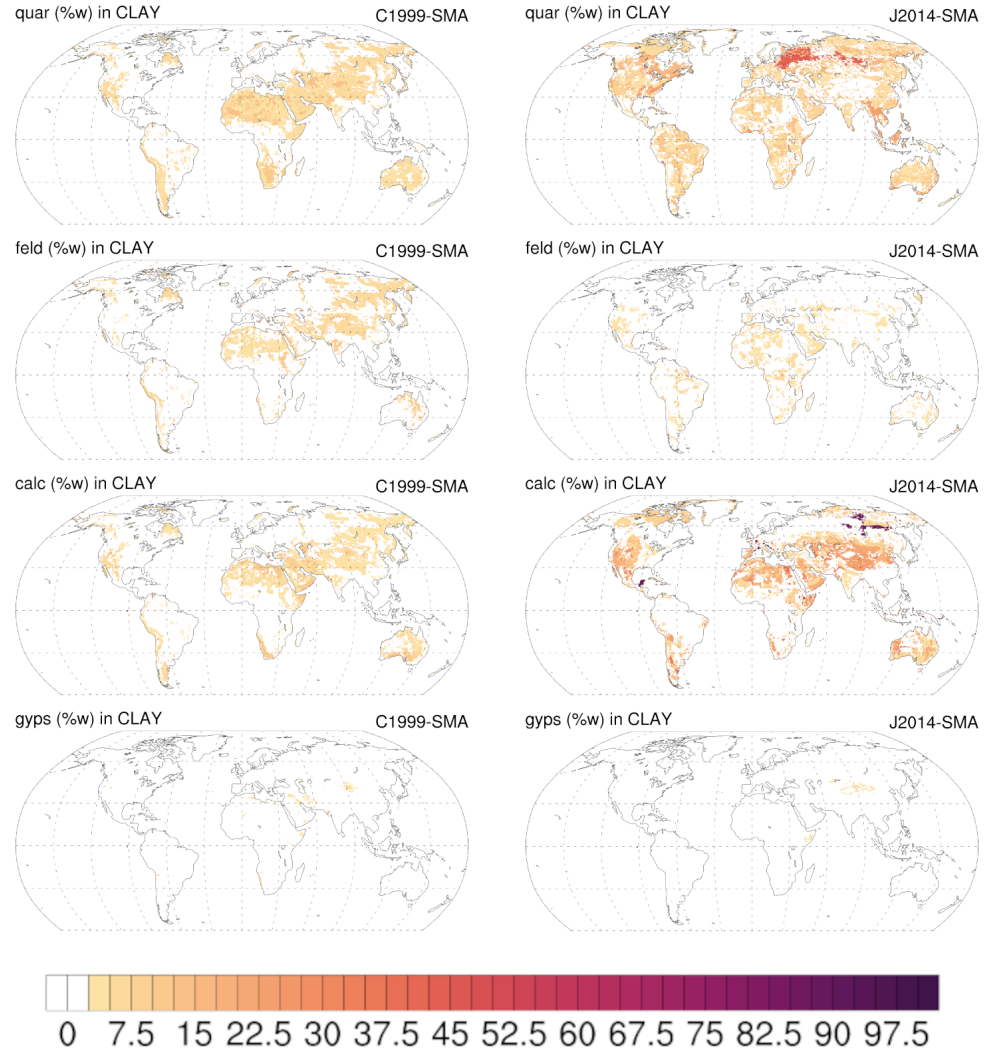


Figure S7. Mass fraction of quartz, feldspars, calcite and gypsum (%w) in the clay sizes of the soil according to C1999-SMA -left- and J2014-SMA -right-.

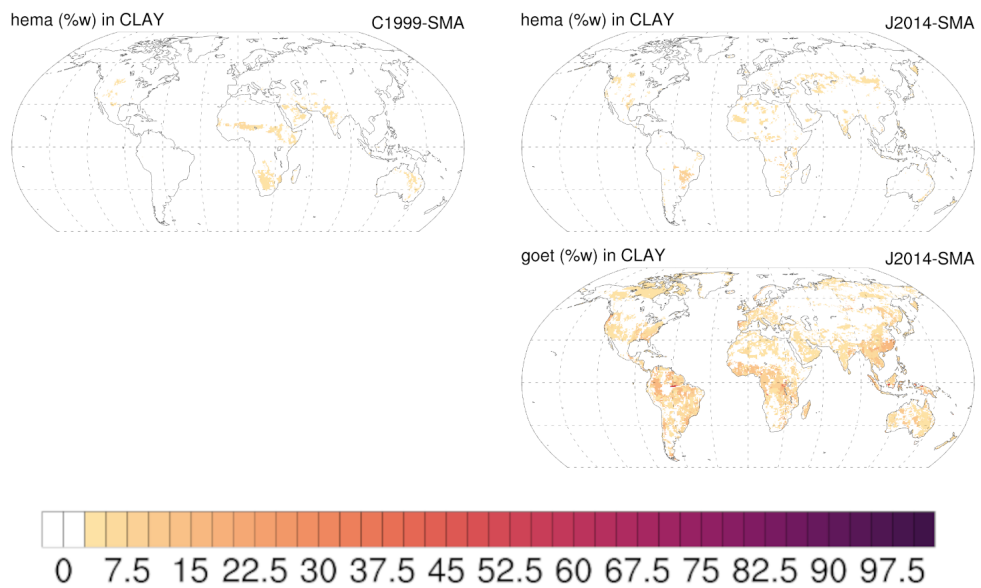


Figure S8. Mass fraction of hematite (iron oxides) and goethite (%w) in the clay sizes of the soil according to C1999-SMA -left- and J2014-SMA -right-.

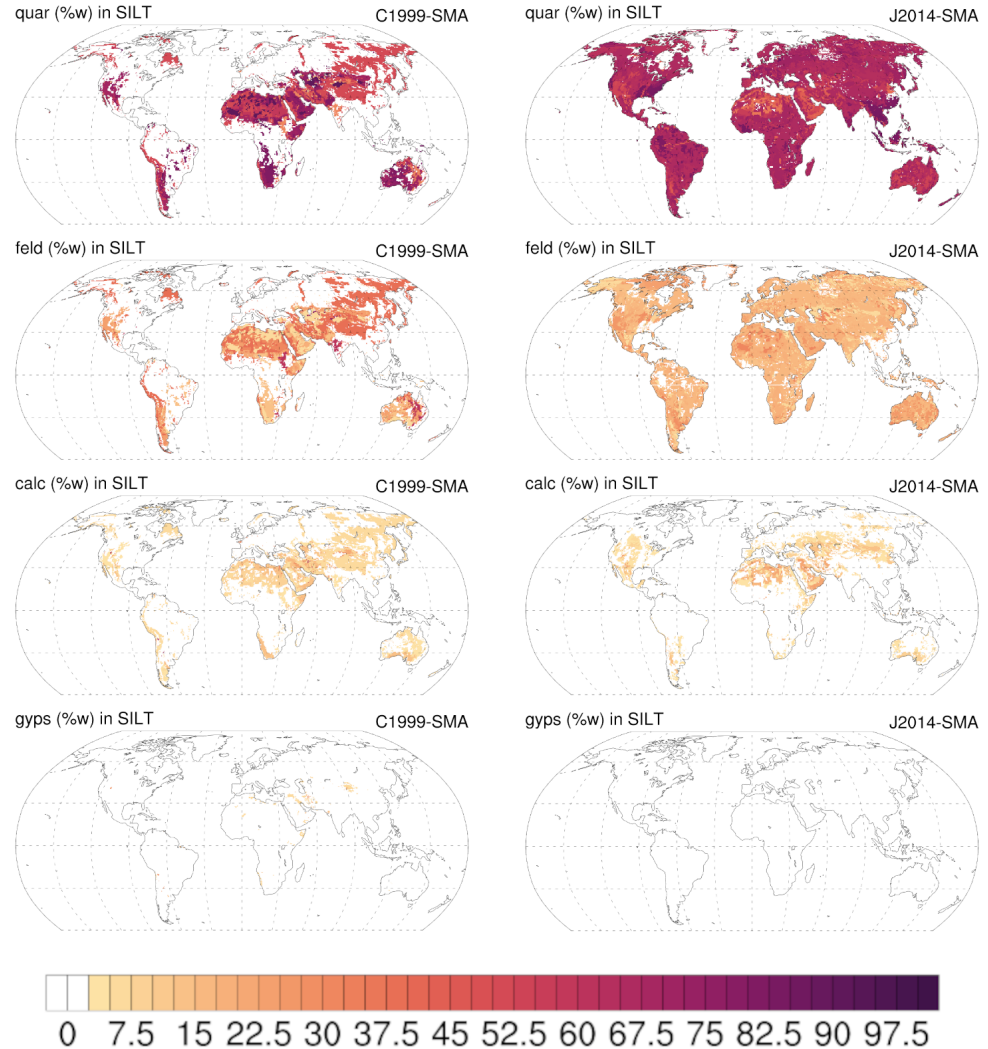


Figure S9. Mass fraction of quartz, feldspars, calcite and gypsum (%w) in the silt sizes of the soil according to C1999-SMA -left- and J2014-SMA -right-.

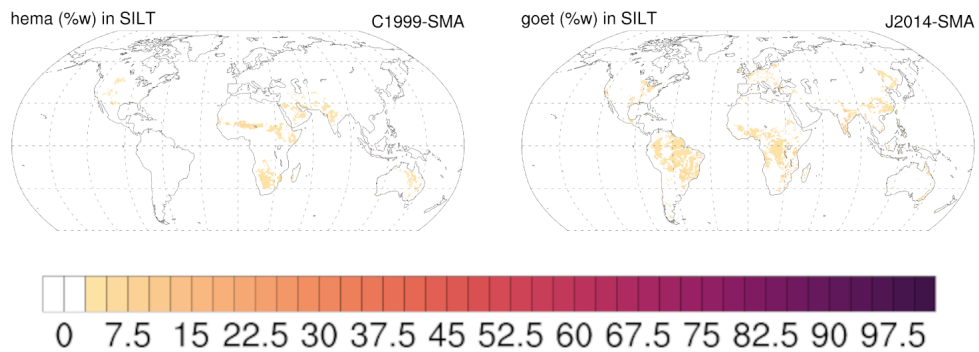


Figure S10. Mass fraction of hematite and goethite (%w) in the silt sizes of the soil according to C1999-SMA -left- and J2014-SMA -right-.

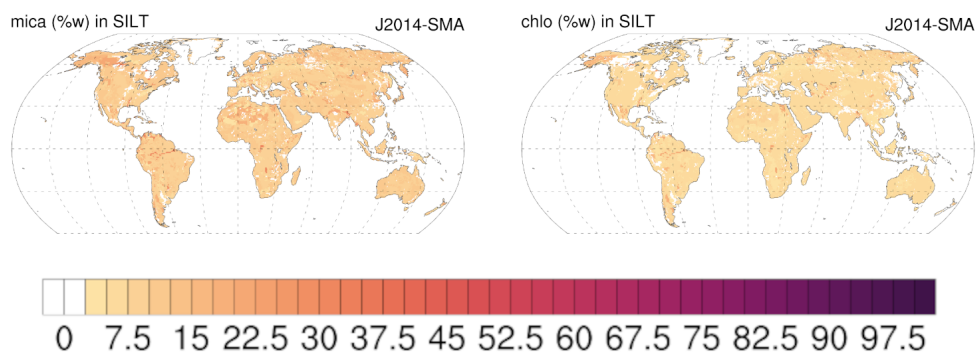


Figure S11. Mass fraction of mica and chlorite (%w) in the silt sizes of the soil according to J2014-SMA.

References

- Albani, S., Mahowald, N. M., Perry, A., Scanza, R. A., Zender, C. S., Heavens, N., Maggi, V., Kok, J. F., and Otto-Btiesner, B.: Improved dust representation in the Community Atmosphere Model, *Journal of Advances in Modeling Earth Systems*, 6, 541–570, <https://doi.org/10.1002/2013MS000279>, 2014.
- 80 Di Biagio, C., Formenti, P., Balkanski, Y., Caponi, L., Cazaunau, M., Pangui, E., Journet, E., Nowak, S., Caquineau, S., Andreae O. M., Kandler, K., Saeed, T., Piketh, S., Seibert, D., Williams, E., and Doussin, J. F. C.: Global scale variability of the mineral dust long-wave refractive index: A new dataset of in situ measurements for climate modeling and remote sensing, *Atmospheric Chemistry and Physics*, 17, 1901–1929, <https://doi.org/10.5194/acp-17-1901-2017>, 2017.
- 85 Di Biagio, C., Formenti, P., Balkanski, Y., Caponi, L., Cazaunau, M., Pangui, E., Journet, E., Nowak, S., Andreae, M. O., Kandler, K., Saeed, T., Piketh, S., Seibert, D., Williams, E., Doussin, J.-F. F., Biagio, C. D., Formenti, P., Balkanski, Y., Caponi, L., Cazaunau, M., Pangui, E., Journet, E., Nowak, S., Andreae, M. O., Kandler, K., Saeed, T., Piketh, S., Seibert, D., Williams, E., Doussin, J.-F. F., Di Biagio, C., Formenti, P., Balkanski, Y., Caponi, L., Cazaunau, M., Pangui, E., Journet, E., Nowak, S., Andreae, M. O., Kandler, K., Saeed, T., Piketh, S., Seibert, D., Williams, E., and Doussin, J.-F. F.: Complex refractive indices and single-scattering albedo of global dust aerosols in the shortwave spectrum and relationship to size and iron content, *Atmospheric Chemistry and Physics*, 19, 15 503–15 531, <https://doi.org/10.5194/acp-19-15503-2019>, 2019.
- 90 Hamilton, D. S., Scanza, R. A., Feng, Y., Guinness, J., Kok, J. F., Li, L., Liu, X., Rathod, S. D., Wan, J. S., Wu, M., and Mahowald, N. M.: Improved methodologies for Earth system modelling of atmospheric soluble iron and observation comparisons using the Mechanism of Intermediate complexity for Modelling Iron (MIMI v1.0), *Geoscientific Model Development*, 12, 3835–3862, <https://doi.org/10.5194/gmd-12-3835-2019>, 2019.
- 95 Myriokefalitakis, S., Ito, A., Kanakidou, M., Nenes, A., Krol, M. C., Mahowald, N. M., Scanza, R. A., Hamilton, D. S., Johnson, M. S., Meskhidze, N., Kok, J. F., Guieu, C., Baker, A. R., Jickells, T. D., Sarin, M. M., Bikkina, S., Shelley, R., Bowie, A., Perron, M. M., and Duce, R. A.: Reviews and syntheses: The GESAMP atmospheric iron deposition model intercomparison study, *Biogeosciences*, 15, 6659–6684, <https://doi.org/10.5194/bg-15-6659-2018>, 2018.
- 100 Perlitz, J. P., Pérez García-Pando, C., and Miller, R. L.: Predicting the mineral composition of dust aerosols - Part 2: Model evaluation and identification of key processes with observations, *Atmospheric Chemistry and Physics*, 15, 11 629–11 652, <https://doi.org/10.5194/acp-15-11629-2015>, 2015.
- Scanza, R. A., Mahowald, N., Ghan, S., Zender, C. S., Kok, J. F., Liu, X., Zhang, Y., and Albani, S.: Modeling dust as component minerals in the Community Atmosphere Model: Development of framework and impact on radiative forcing, *Atmospheric Chemistry and Physics*, 15, 537–561, <https://doi.org/10.5194/acp-15-537-2015>, 2015.
- 105 Sinyuk, A., Torres, O., and Dubovik, O.: Combined use of satellite and surface observations to infer the imaginary part of refractive index of Saharan dust, *Geophysical Research Letters*, 30, 1081, <https://doi.org/10.1029/2002GL016189>, 2003.